9-1-2023

TOI-908: A Planet At The Edge Of The Neptune Desert Transiting A G-Type Star

F. Hawthorn

D. Bayliss

D. J. Armstrong

See next page for additional authors

Authors

F. Hawthorn, D. Bayliss, D. J. Armstrong, J. Fernández Fernández, A. Osborn, S. G. Sousa, V. Adibekyan, J. Davoult, K. A. Collins, Y. Alibert, S. C. C. Barros, F. Bouchy, M. Brogi, D. R. Ciardi, T. Daylan, E. Delgado Mena, O. D. S. Demangeon, R. F. Díaz, T. Gan, K. Horne, S. Hoyer, J. M. Jenkins, Eric L.N. Jensen, J. F. Kielkopf, V. Kostov, D. W. Latham, A. M. Levine, J. Lillo-Box, L. D. Nielsen, H. P. Osborn, G. R. Ricker, J. Rodrigues, N. C. Santos, R. P. Schwarz, S. Seager, J. Serrano Bell, A. Shporer, C. Stockdale, P. A. Strøm, P. Tenenbaum, S. Udry, P. J. Wheatley, J. N. Winn, and C. Ziegler

TOI-908: a planet at the edge of the Neptune desert transiting a G-type star

Faith Hawthorn [1,2]★ Daniel Bayliss [1,2]★ David J. Armstrong [1,2]★ Jorge Fernández Fernández [1,2]
Ares Osborn [1,2] Sérgio G. Sousa [3,4] Vardan Adibekyan,[3,4] Jeanne Davoult,[5] Karen A. Collins [6]
Yann Alibert,[5] Susana C. C. Barros,[3,4] François Bouchy,[7] Matteo Brogi,[1,2,8] David R. Ciardi,[9]
Tansu Daylan,[10] Elisa Delgado Mena,[3] Olivier D. S. Demangeon [3,4] Rodrigo F. Díaz,[11] Tianjun Gan,[12]
Keith Horne,[13] Sergio Hoyer [14] Jon M. Jenkins,[15] Eric L. N. Jensen [16] John F. Kielkopf,[17]
Veselin Kostov,[18] David W. Latham,[6] Alan M. Levine,[19] Jorge Lillo-Box,[20] Louise D. Nielsen,[21]
Hugh P. Osborn,[5,19] George R. Ricker,[19] José Rodrigues,[3,4] Nuno C. Santos,[3,4] Richard P. Schwarz,[6]
Sara Seager,[19,22,23] Juan Serrano Bell,[24] Avi Shporer,[19] Chris Stockdale,[25] Paul A. Strøm,[1,2]
Peter Tenenbaum,[15,26] Stéphane Udry,[7] Peter J. Wheatley [1,2] Joshua N. Winn[10] and Carl Ziegler[27]

Affiliations are listed at the end of the paper

ABSTRACT

We present the discovery of an exoplanet transiting TOI-908 (TIC-350153977) using data from *TESS* sectors 1, 12, 13, 27, 28, and 39. TOI-908 is a $T = 10.7$ mag G-dwarf ($T_{\text{eff}} = 5626 \pm 61$ K) solar-like star with a mass of $0.950 \pm 0.010 \, M_{\odot}$ and a radius of $1.028 \pm 0.030 \, R_{\odot}$. The planet, TOI-908 b, is a $3.18 \pm 0.16 \, R_{\oplus}$ planet in a 3.18 d orbit. Radial velocity measurements from *HARPS* reveal TOI-908 b has a mass of approximately $16.1 \pm 4.1 \, M_{\oplus}$, resulting in a bulk planetary density of $2.7^{+0.2}_{-0.4} \, \text{g cm}^{-3}$. TOI-908 b lies in a sparsely populated region of parameter space known as the Neptune desert. The planet likely began its life as a sub-Saturn planet before it experienced significant photoevaporation due to X-rays and extreme ultraviolet radiation from its host star, and is likely to continue evaporating, losing a significant fraction of its residual envelope mass.

Key words: techniques: photometric – techniques: radial velocities – planets and satellites: detection – stars: individual: TOI-908 (TIC-350153977, GAIA DR3 46192380870592067842).

1 INTRODUCTION

In the years since *Kepler* (Borucki et al. 2010) and during the lifetime of the *TESS* mission (Ricker et al. 2015), a distinct dearth of exoplanets between $3 < R_{\oplus} < 4$ with orbital periods less than ~ 5 d has been discovered, the so-called 'Neptune desert,' 'evaporation desert,' or 'sub-Jovian desert' (Szabó & Kiss 2011; Mazeh, Holczer & Faigler 2016; Owen & Lai 2018a). Several theories have been made to explain this sparse parameter space – including that these relatively low-mass planets have had their gaseous H/He envelopes stripped away by high levels of irradiation from their host stars (Owen & Wu 2017), leaving behind a dense core (e.g. TOI-849 b; Armstrong et al. 2020), while some are still undergoing this process (e.g. NGTS-4 b, West et al. 2019; LTT 9779 b, Jenkins et al. 2020; TOI-969 b, Lillo-Box et al. 2022).

Many of these planets are readily observable with missions such as *TESS* and *JWST*, and also with ground-based spectroscopic instruments such as *HARPS* (Mayor et al. 2003) and *ESPRESSO* (Pepe et al. 2021) due to their close orbits and short periods. The

HARPS-NOMADS programme (PI: Armstrong, 1108.C-0697) aims to significantly increase the number of planet confirmations in the Neptune desert with precise masses and radii. In this paper, we present one such detection of TOI-908 b, a sub-Neptune transiting a G-type star. Precise measurements of these parameters is highly important in allowing us to constrain the density and internal structure of these planets, assisting in our understanding of the formation and evolution mechanisms that place these planets in the desert.

This paper is structured as follows: we present our observations of TOI-908 from *TESS* and *LCOGT* photometry, *HARPS* spectroscopy and *SOAR*-HRCam imaging in Section 2, our stellar analysis and global joint modelling of the data in Section 3, and our results and discussion of our findings in Section 4, including the position of the planet in the Neptune desert and the evolution of its envelope. We finally present our conclusions in Section 5.

2 OBSERVATIONS

2.1 *TESS* photometry

TESS is a space-based NASA telescope that is currently performing a survey search for transiting exoplanets around bright host stars. It is equipped with four cameras for a total combined FOV (field of

Table 1. Stellar parameters of TOI-908.

Property	Value	Source
Identifiers		
TIC ID	TIC-350153977	TICv8
2MASS ID	J03323821-81150267	*2MASS*
Gaia ID	46192380870592067842	*Gaia* DR3
Astrometric properties		
RA (J2015.5)	$03^h32^m38\overset{s}{.}26$	*Gaia* DR3
Dec. (J2015.5)	$-81°15'02\overset{''}{.}68$	*Gaia* DR3
Parallax (mas)	5.686 ± 0.010	*Gaia* DR3
Distance (pc)	$175.70^{+4.22}_{-0.59}$	*Gaia* DR3
μ_{RA} (mas yr^{-1})	5.898 ± 0.013	*Gaia* DR3
μ_{Dec} (mas yr^{-1})	-0.353 ± 0.015	*Gaia* DR3
μ_{Total} (mas yr^{-1})	5.909 ± 0.012	*Gaia* DR3
RV_{sys} (km s^{-1})	9.071 ± 0.347	*Gaia* DR3
Gaia non-single star flag	0^a	*Gaia* DR3
Photometric properties		
TESS (mag)	10.651 ± 0.006	TICv8
B (mag)	12.005 ± 0.169	*APASS*
V (mag)	11.316 ± 0.012	*APASS*
G (mag)	11.1061 ± 0.0004	*Gaia* DR3
J (mag)	10.04 ± 0.02	TICv8
H (mag)	9.734 ± 0.026	TICv8
K (mag)	9.637 ± 0.021	TICv8
Gaia BP (mag)	11.4711 ± 0.0009	*Gaia* DR2
Gaia RP (mag)	10.6024 ± 0.8146	*Gaia* DR2

Sources: TICv8 (Stassun et al. 2019), *2MASS* (Skrutskie et al. 2006), *Gaia* Data Release 3 (Brown et al. 2018), *APASS* (Henden et al. 2016), *Gaia* Data Release 2 (Gaia Collaboration 2018).

^{a}Indicates that the star does not belong to an astrometric, spectroscopic, or eclipsing binary.

view) of $24° \times 96°$. It splits the sky into 13 sectors per hemisphere, each of which is observed for approximately 27 d, making *TESS* a key mission in detecting short-period transiting exoplanets. *TESS* observed the bright star TOI-908 (TIC-350153977) in sectors 1, 12, and 13 during Cycle 1 of operation (2018-07-25 to 2019-07-17) at a cadence of 30 min, and sectors 27, 28, and 39 during Cycle 3 (2020-07-05 to 2021-06-24) at a cadence of 10 min. The target location at a declination of approximately $-81°$ means it lies close to the *TESS* Continuous Viewing Zone (CVZ), and therefore also close to the CVZ of *JWST*. TOI-908 is a $T = 10.7$ mag G-dwarf with an effective temperature of 5626 ± 61 K (see Section 3.1). Details of TOI-908 including identifiers, astrometric and photometric properties are presented in Table 1, and a full list of the *TESS* sector details are set out in Table 2. We present the Target Pixel File (TPF; created with tpfplotter[1] from Aller et al. 2020) in Fig. 1 with TOI-908 as the central object with *Gaia* DR2 sources, scaled magnitudes for each object ranked by distance from TOI-908 and the aperture mask used for photometry extraction with a TIC contamination ratio of 0.040531.

The candidate was alerted as a TOI (*TESS* Object of Interest; Guerrero et al. 2021) and designated TOI-908.01 (hereafter TOI-908 b), based on the identification of a 3.18 d transit signal from the SPOC pipeline (Jenkins 2002; Jenkins et al. 2010, 2020). This pipeline uses the PDCSAP (Presearch Data Conditioning Simple Aperture Photometry; Smith et al. 2012; Stumpe et al. 2012, 2014) light curves from the *TESS* HLSP (High Level Science Products), which removes instrumental and some stellar trends from the SAP

(Simple Aperture Photometry) data, but retains local features such as transits. The transits of TOI-908 b passed the diagnostic tests after fitting with a limb-darkened transit model (Li et al. 2019) and were reported in the Data Validation Report (Twicken et al. 2018). The PDCSAP light curves are used in the joint model described in Section 3.2. We present the normalized light curves from each Sector of *TESS* along with the generated best-fitting transit models for TOI-908 b in Fig. 2.

2.2 LCOGT follow-up photometry

The *LCOGT* (Las Cumbres Observatory Global Telescope network; Brown et al. 2013) was used to take a total of five time-series transit photometry observations of TOI-908, each of which is detailed in Table 2. We used the TESS TRANSIT FINDER, which is a customized version of the TAPIR software package (Jensen 2013), to schedule our transit observations. Each of the telescopes has a 26 arcmin × 26 arcmin FOV from 4096 × 4096 SINISTRO cameras with an image scale of 0.389 arcsec pix^{-1}, and observations were taken in the SDSS *i'* and PanSTARRS *z*-short bands. The *LCOGT* image data were processed using the standard BANZAI data reduction pipeline presented in McCully et al. (2018), and photometric data were extracted with the ASTROIMAGEJ analysis software detailed in Collins et al. (2017) using circular photometric apertures with radii 7.0 arcsec or smaller, which exclude flux from the nearest known *Gaia* DR3 star 13.5 arcsec northwest of TOI-908. Parametric detrending vectors were selected by jointly fitting a transit model and linear combinations of zero, one, or two detrending parameters from the available detrending vectors airmass, time, sky-background, full width at half-maximum (FWHM), *x*-centroid, *y*-centroid, and total comparison star counts (a proxy for atmospheric losses). The best zero, one, or two detrend vectors were retained if they improved the Bayesian information criterion (BIC) for the fit by at least a factor of 2 per detrend parameter. The detrending vectors selected for each light curve are shown in Table 2. The *LCOGT* light-curves are used in the joint model in Section 3.2. A ~900 ppm transit-like event was detected in the follow-up light curves (see Section 4), confirming that the *TESS*-detected signal occurs on TOI-908 relative to known *Gaia* DR3 stars. The *LCOGT* data are publicly available on the ExoFOP-*TESS* website.[2] We present the light curves and best-fitting transit models from *LCOGT* in Fig. 3.

2.3 HARPS radial velocity observations

We obtained 42 spectra with the high accuracy radial velocity planet searcher (*HARPS*; Mayor et al. 2003). *HARPS* is an echelle spectrograph mounted on the 3.6 m ESO telescope at La Silla Observatory, Chile, capable of stabilized high-resolution measurements ($R \sim 115\,000$) at $\sim$1 m s^{-1} precision (Mayor et al. 2003). These spectra were obtained through the *HARPS*-NOMADS programme (PI: Armstrong, 1108.C-0697) from 2021-10-15 to 2022-01-26 in high accuracy mode (HAM) with a fibre diameter of 1 arcsec and an exposure time of 1800 s, leading to a typical signal to noise of 40–50 per pixel at a wavelength of 550 nm. The raw *HARPS* data are processed using the standard data reduction pipeline presented in Lovis & Pepe (2007) using the G2 spectral mask, which also includes measurements of the FWHM, the line bisector span, the contrast of the cross-correlation function (CCF) and the standard activity indicators of S, H α, Na, and Ca indices.

[1] https://github.com/jlillo/tpfplotter

[2] https://exofop.ipac.caltech.edu/tess/

Table 2. Photometric observations of TOI-908.

Instrument	Aperture	Filter	Exposure time (s)	Number of images	UT night	Detrending	TTV (mins)
TESS S01	0.105 m	*TESS*[a]	1800	1337	2018 Jul 25–2018 Aug 22	GP model	$-0.2^{+2.4b}_{-2.2}$
TESS S12	0.105 m	*TESS*	1800	1340	2019 May 21–2019 Jun 18	GP model	$5.2^{+2.8}_{-4.3}$
TESS S13	0.105 m	*TESS*	1800	1365	2019 Jun 19–2019 Jul 17	GP model	$-0.2^{+2.2}_{-2.6}$
LCOGT-CTIO	1.0 m	z_s[c]	35	302	2019 Sep 08	Time, losses	$-12.3^{+4.2}_{-3.8}$
LCOGT-SAAO	1.0 m	z_s	35	252	2019 Dec 31	Time, losses	$-8.2^{+8.8}_{-6.7}$
TESS S27	0.105 m	*TESS*	600	3508	2020 Jul 05–2020 Jul 30	GP model	$-7.3^{+2.7}_{-3.2}$
TESS S28	0.105 m	*TESS*	600	3636	2020 Jul 31–2020 Aug 25	GP model	$4.7^{+4.3}_{-1.3}$
LCOGT-SAAO	1.0 m	z_s	35	227	2020 Sep 17	Airmass	$-17.3^{+9.5}_{-4.5}$
LCOGT-CTIO	1.0 m	z_s	35	176	2020 Nov 30	x-centroid	$-7.5^{+14.2}_{-7.8}$
LCOGT-CTIO	1.0 m	i_p[d]	20	308	2020 Dec 16	x-centroid, losses	$-5.1^{+8.8}_{-10.9}$
TESS S39	0.105 m	*TESS*	120	4024	2021 May 27	GP model	$0.9^{+1.3}_{-3.1}$

[a]*TESS* custom, 600–1000 nm. [b]Average TTV per *TESS* sector, calculated using $T_c = 2384.292 \pm 0.002$ TBJD and $P = 3.183792 \pm 0.000007$ d. See Table A6 for full table of *TESS* TTVs. [c]PanSTARRS *z*-short, $\lambda_{mid} = 8700$ nm, $\delta\lambda = 1040$ nm. [d]SDSS *i'*, $\lambda_{mid} = 7545$ nm, $\delta\lambda = 1290$ nm.
Notes. CTIO – Cerro Tololo Inter-American Observatory. SAAO – South Africa Astronomical Observatory.
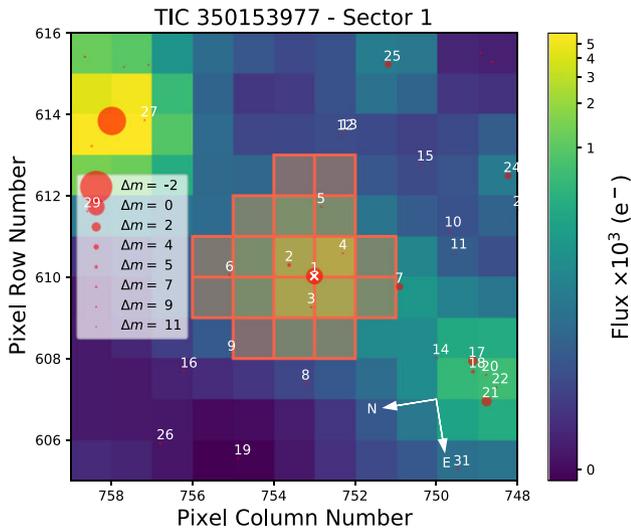
Figure 1. Target pixel file (TPF) from *TESS* sector 1 with TOI-908 marked with a white cross. Other sources from *Gaia* DR2 are marked with red circles sized by scaled magnitudes relative to the target, ranked by distance. The aperture mask is indicated by the red outline.

It should also be noted that these data were obtained at relatively higher airmasses (∼1.66) due to the on-sky position and the low declination of the target. These data are used in the radial velocity (RV) component of our joint model (Section 3.2), and the data are presented in Table 3. Our radial velocity data from *HARPS* is shown in its entirety in Fig. 4 along with the fitted GP model and residuals, and the same data phase folded to the period of TOI-908 b is displayed in Fig. 5. We present the Lomb–Scargle periodograms of the data presented in Table 3 in Fig. 7 and compare each to the orbital period and period aliases of TOI-908 b. The periodograms of the additional activity indicators mentioned previously and their values are presented in Fig. A1 and Table A5, respectively. We find additional periodicities above the 1 per cent false alarm probability (FAP) line in the CCF contrast, *S* index, Na index, and Ca index; however, due to the large uncertainty in the fitted stellar rotational period we cannot attribute these periodicities to this feature, and we encourage further monitoring of the spectroscopic radial velocity of the system.

2.4 SOAR-HRCam speckle imaging

To check for stellar companions to TOI-908 that may be blended into the photometric data due to the comparatively large *TESS* pixel scale of 21 arcsec, *SOAR* (*SOuthern Astrophysical Research* telescope; Tokovinin 2018) speckle imaging observations of the target were taken on 2019-10-16 in the Cousins-*I* filter at a resolution of 36 mas (Ziegler et al. 2020). We show the 5σ sensitivity limit and autocorrelation functions (ACFs) for the observations in Fig. 6, and detect no contaminating sources within 3 arcsec of the target.

3 ANALYSIS

3.1 Stellar analysis

To derive the stellar spectroscopic parameters (T_{eff}, log g, microturbulence, [Fe/H]), we used ARES + MOOG following the same methodology described in Santos et al. (2013), Sousa (2014), and Sousa et al. (2021). The latest version of ARES[3] (Sousa et al. 2007, 2015) was used to measure the equivalent widths (EWs) of iron lines on the combined spectrum of TOI-908. We then use a minimization process to find ionization and excitation equilibrium and converge to the best set of spectroscopic parameters. This process makes use of a grid of Kurucz model atmospheres (Kurucz 1993a) and the radiative transfer code MOOG (Sneden 1973a). We also derived a more accurate trigonometric surface gravity using recent *Gaia* data following the same procedure as described in Sousa et al. (2021).

Stellar abundances of the elements were derived using the classical curve-of-growth analysis method assuming local thermodynamic equilibrium and with the same codes and models that were used for the stellar parameters determinations. For the derivation of chemical abundances of refractory elements, we closely followed the methods described in Adibekyan et al. (2012, 2015) and Delgado Mena et al. (2017). Abundances of the volatile elements, C and O, were derived following the method of Bertran de Lis et al. (2015) and Delgado Mena et al. (2021). All the abundance ratios [X/H] are obtained by doing a differential analysis with respect to a high S/N solar (Vesta) spectrum from *HARPS*. The final

[3]The latest version, ARES v2, can be downloaded at https://github.com/sousasag/ARES.
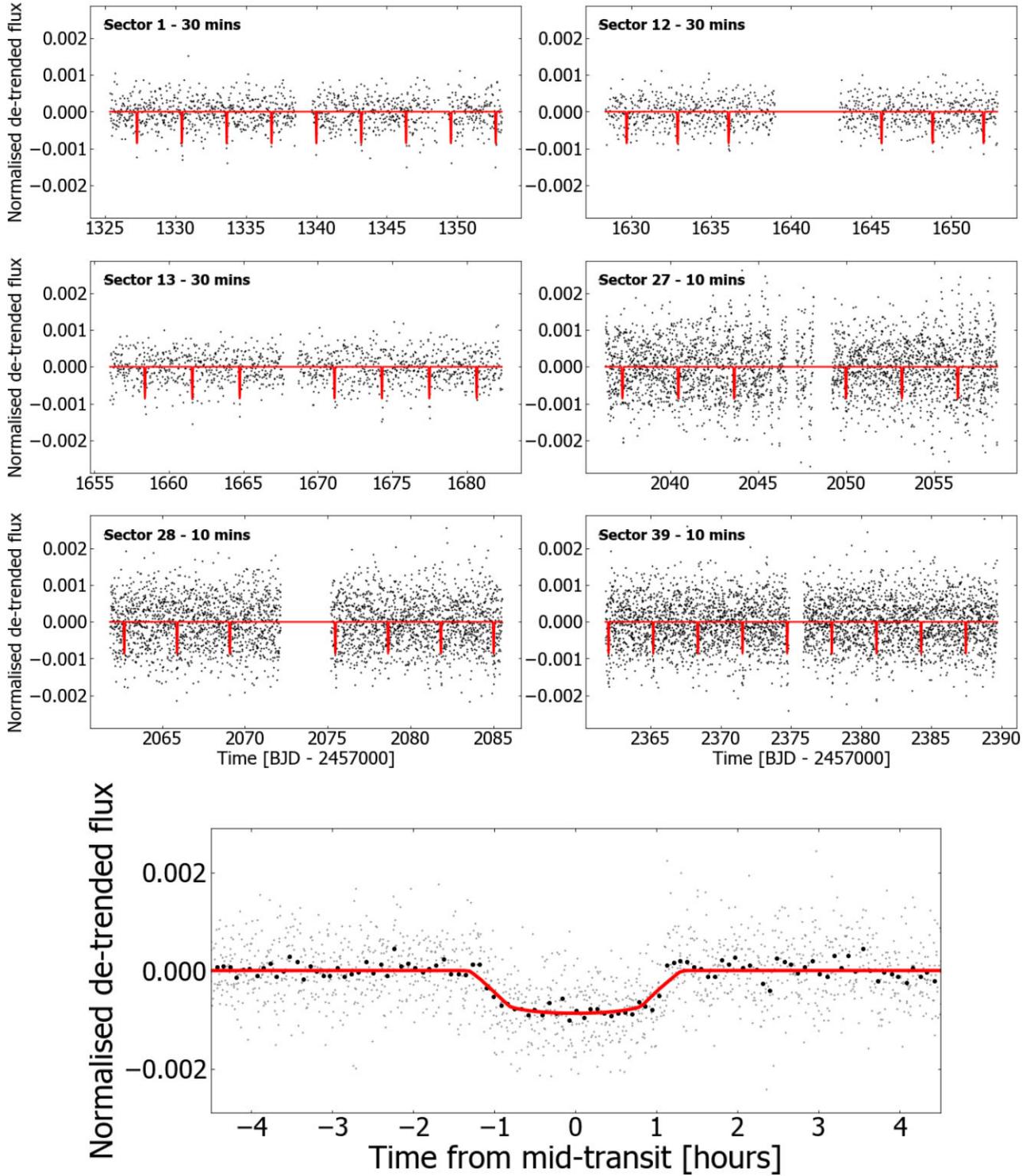
Figure 2. *Top panels: TESS* PDCSAP light curves from labelled sectors at labelled cadences with the GP model removed, overplotted with the best-fitting transit models for TOI-908 b in red. *Bottom panel: TESS* PDCSAP lightcurves from all sectors (grey points), phase folded to a period corresponding to that of TOI-908 b overplotted with the best-fitting transit model in red and binned to 10 min intervals (black points).

abundances, shown in Table 4, are typical of a galactic thin-disc star. Moreover, we used the chemical abundances of some elements to derive ages through the so-called chemical clocks (i.e. certain chemical abundance ratios which have a strong correlation for age). We applied the 3D formulas described in table 10 of Delgado Mena

et al. (2019), which also consider the variation in age produced by the effective temperature and iron abundance. The chemical clocks [Y/Mg], [Y/Zn], [Y/Ti], [Y/Si], [Y/Al], [Sr/Ti], [Sr/Mg], and [Sr/Si] were used from which we obtain a weighted average age of 4.6 ± 1.5 Gyr.
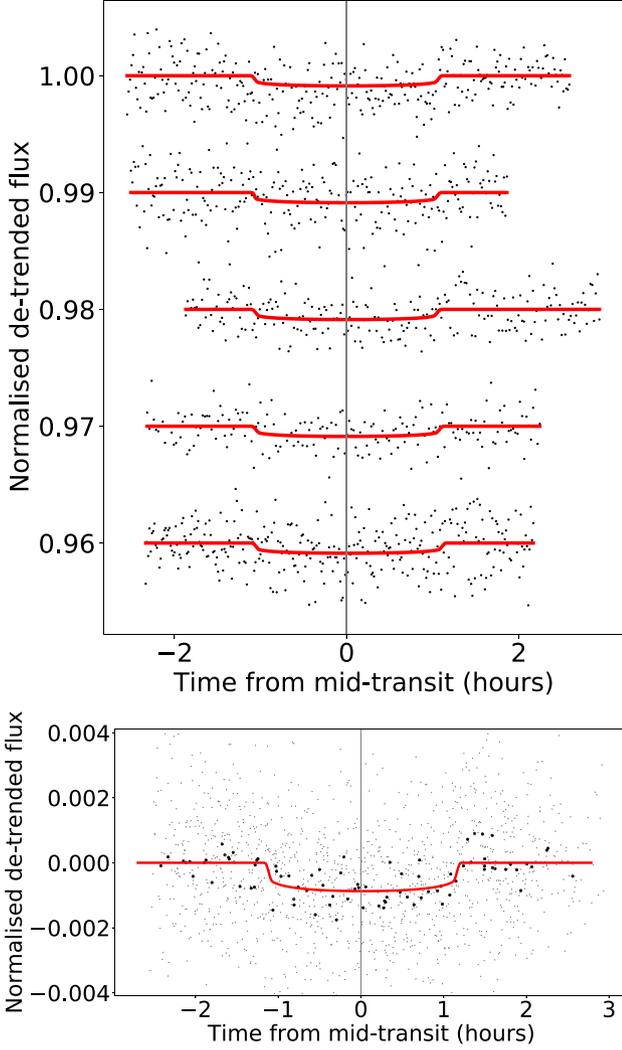
Figure 3. *Top panel:* Photometric observations of TOI-908 taken by the *LCOGT* facilities as detailed in Table 2 in order of observation date from top to bottom, overplotted with the best-fitting transit models in red, and offset vertically for clarity. *Bottom panel:* All *LCOGT* light curves (grey points), phase folded to a period corresponding to that of TOI-908 b, overplotted with the best-fitting transit model in red and binned to 10 min intervals (black points).

3.2 Joint modelling

We use the EXOPLANET (Foreman-Mackey et al. 2021a; Foreman-Mackey et al. 2021c) code framework to jointly model the photometric and spectroscopic data for TOI-908 detailed in Section 2. EXOPLANET incorporates the packages STARRY (Luger et al. 2019a), PYMC3 (Salvatier, Wiecki & Fonnesbeck 2016a), and CELERITE (Foreman-Mackey et al. 2017). Our photometry data subset contains all observations presented in Table 2, and our RV data subset consists of the *HARPS* observations presented in Section 2.3, all of which have been converted to the TBJD time system (*TESS* Barycentric Julian Date; BJD – 2457000) for uniformity. To create a complete model that incorporates all observations and the GP (Gaussian Process) models for each, outlined further in Sections 3.2.1 and 3.2.2, we obtain our initial fit values from the maximum log probability of the PYMC3 model, and then use these values as the starting point to draw samples from the posterior distribution using a NUTS (No U-Turn

Sampler) variant of the HMC (Hamilton Monte Carlo; Hoffman & Gelman 2011) algorithm. We use a burn-in of 4000 samples which are discarded, 4000 steps and 10 chains, which gives our model good convergence without excessive computation time. The prior distributions implemented and their resulting fit values can be found in Table A1 for TOI-908 and Table A2 for TOI-908 b. The priors and resulting fit values for the *TESS* GP parameters can be found in Table A3.

3.2.1 Light-curve detrending

To remove residual effects of stellar variability on the *TESS* light curves that were not fully removed by the PDCSAP algorithm, we use a GP (Gaussian Process) model on each of the six Sectors of data using the CELERITE and PYMC3 packages. This GP model is defined by three hyper-parameters for each *TESS* Sector, with $\log(s2)$ describing the excess white noise in the data, and $\log(\omega0)$ and $\log(S\omega4)$ representing the non-periodic components of stellar variability in the light-curves (Salvatier et al. 2016a). These parameters are passed into the SHOTerm kernel in the EXOPLANET framework, which represents a stochastically driven simple harmonic oscillator Foreman-Mackey et al. (2021a). The effect of these GP models can be seen in Fig. A2, and the corresponding equation is presented in equation (1), where $S_0\omega_0^4$ represents the $S\omega4$ term as described above and $Q = \frac{1}{\sqrt{2}}$,

$$S(\omega) = \sqrt{\frac{2}{\pi}} \frac{S_0\omega_0^4}{\left(\omega^2 - \omega_0^2\right)^2 + \omega_0^2\omega^2/Q}. \tag{1}$$

We normalize each of our follow-up photometry observations from *LCOGT* by dividing each light-curve by the median of the out-of-transit flux and subtracting the mean of the out-of-transit flux. We find no need to apply a GP model to these light-curves due to the shorter baselines of the observations over the course of a single transit.

Each of the transits from the photometry data are modelled within the EXOPLANET code as a Keplerian orbit following the formalization of Kipping (2013b), defined by the stellar parameters of radius (R_*) and mass (M_*) in Solar units, and the planetary parameters of orbital period (P) in days, central transit ephemeris (T_c) in TBJD (BJD-2457000), impact parameter (b), eccentricity (e), and argument of periastron (ω) in radians, including the limb-darkening coefficients u_1 and u_2. A set of transit models for each data set is generated using the STARRY package contained in EXOPLANET, which also incorporates the planetary radius (R_p) and exposure times for each instrument (see Table 2).

3.2.2 Radial velocity (RV) detrending

We first examine the *HARPS* radial velocity data (RMS 0.0048, mean error 2.79 m s^{-1}) using the DACE[4] platform, in which we find two significant periodic signals above the level of the 1 per cent analytical FAP that are not aliases of each other (Fig. 8). We find the planetary signal of TOI-908 b on a period of 3.182 d with a predicted radial velocity semi-amplitude K of 7.72 m s^{-1}, and a secondary periodic signal at 19.29 d with a semi-amplitude of 7.25 m s^{-1} after removal of the planetary signal in DACE. We also calculate a rotational period of $20.53^{+6.77}_{-4.06}$ d based on a measured $v\sin i_*$ of 2.56 ± 0.64 km s^{-1} (Table 4, Section 3.1), and as the peak periodic signal from DACE falls within this tolerance, we attribute it to stellar rotational modulation (P_{rot}).

---

[4]DACE is accessible at: https://dace.unige.ch/.
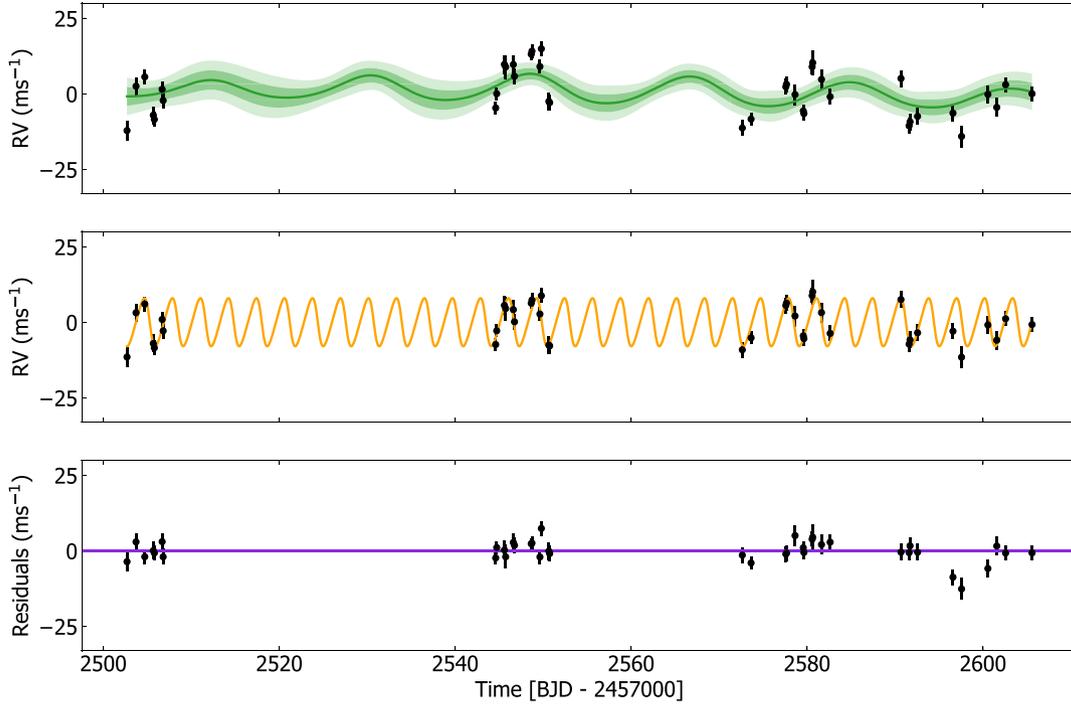
Figure 4. *Top panel: HARPS* radial velocity data for TOI-908 (black circles) with formal uncertainties, and the GP model plotted in green with 1 and 2 standard deviations from the model either side. *Middle panel:* Radial velocity model of TOI-908 b (orange) with the GP model subtracted, overplotted with the *HARPS* datapoints. *Bottom panel:* Residuals for the *HARPS* data.
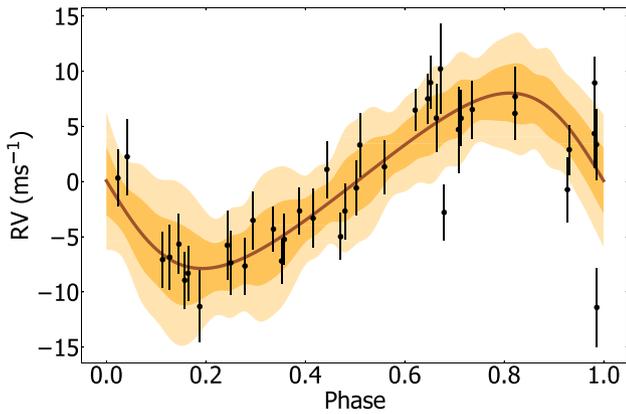
Figure 5. *HARPS* radial velocity data for TOI-908, phase folded to a period corresponding to that of TOI-908 b and overplotted with the model in orange with 1 and 2 standard deviations from the model either side.

As with the photometric *TESS* data, we also apply a GP model to the *HARPS* data to account firstly for the stellar rotational period, and secondly for any residual instrumental or noise effects that are not accounted for in the data reduction. The prior for $P_{\rm rot}$ is set up as a normal distribution around the predicted value of 20.53 d with a standard deviation of 7 d (Table A1), based on the analysis from DACE. Our quasi-periodic GP kernel used is identical to that of Hawthorn et al. (2022) and Osborn et al. (2021), which is a combination of the PERIODIC and EXPQUAD (squared exponential) kernels available from the PYMC3 package (Salvatier, Wiecki & Fonnesbeck 2016b), multiplied to create our final kernel in equation (2). This final kernel is parameterised by the GP amplitude η, the stellar rotation period $P_{\rm rot}$, the time-scale of active region evolution

l_E and the smoothing parameter l_P:

$$k(x, x') = \eta^2 \exp\left(-\frac{\sin^2(\pi|x - x'|\frac{1}{P_{\rm rot}})}{2l_P^2} - \frac{(x - x')^2}{2l_E^2}\right). \qquad (2)$$

We first find predicted values for the radial velocity of TOI-908 b at each timestamp in the *HARPS* data, which uses a uniform prior between 0 and $10\,\mathrm{m\,s^{-1}}$ for the semi-amplitude K of the planet signal. We also fit for the instrumental offset of *HARPS* to account for the differences in RV zero-points between instruments, and any other residual effects not incorporated into the *HARPS* formal uncertainties or the GP model. Our noise model adds jitter noise in quadrature with the nominal RV uncertainties in equation (3),

$$\sigma^2 = \sigma_0^{\,2} + \sigma_i^{\,2}, \qquad (3)$$

where σ_0 is the RMS of the jitter noise and σ_i is the nominal uncertainty of the ith radial velocity measurement. The priors and resulting fit values for the *HARPS* radial velocity GP can be found in Table A4.

4 RESULTS AND DISCUSSION

The results of our joint modelling show that TOI-908 b is a sub-Neptune with a mass of $16.1 \pm 4.1\,\mathrm{M_\oplus}$ and a radius of $3.18 \pm 0.16\,\mathrm{R_\oplus}$ orbiting a G-dwarf star in a close-in 3.18 d orbit. Our final set of parameters for TOI-908 b can be found in Table 5.

4.1 Density

In Fig. 9, we plot the position of TOI-908 b relative to the sample of planets from the *TEPCAT* catalogue (Southworth 2011), and relative to composition models obtained from (Zeng et al. 2016) using the

Table 3. *HARPS* spectroscopic data for TOI-908. This table is available in its entirety online.

Time (BJD −2457000)	RV (m s^{-1})	RV error (m s^{-1})	FWHM (m s^{-1})	FWHM error (m s^{-1})	Bisector (m s^{-1})	Bisector error (m s^{-1})	Contrast	Contrast error	S-index$_{MW}$	S-index$_{MW}$ error
2502.6901	9091.80	3.25	7074.23	10.00	−21.19	4.60	49.379401	0.000001	0.15	0.01
2503.7151	9106.48	2.92	7080.40	10.01	−19.09	4.12	49.346258	0.000001	0.15	0.01
2504.7080	9109.55	2.43	7067.72	10.00	−20.01	3.43	49.306873	0.000001	0.16	0.01
2505.6817	9096.90	2.92	7063.40	9.989	−30.19	4.13	49.292743	0.000001	0.14	0.01
2505.7989	9095.50	2.50	7067.65	10.00	−31.01	3.53	49.280238	0.000001	0.16	0.01
...	...	...	...	...	...	...	...	...	...	...
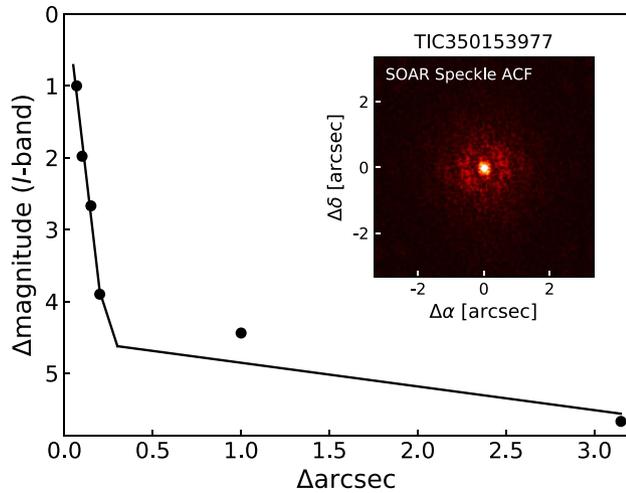
Figure 6. *SOAR* speckle imaging observations (insert), 5σ sensitivity limit, and autocorrelation functions (ACF) of TOI-908, showing no detection of close companions within 3 arcsec of the target.

open-source code FANCY-MASSRADIUS-PLOT[5] TOI-908 b sits above the 100 per cent water planetary composition model amongst a more sparse population. The mass, radius and resulting bulk density of TOI-908 b (Table 5) is similar to that of other known hot Neptune planets.

4.2 Position of the planet in the Neptune desert

In Fig. 10, we plot the position of TOI-908 b relative to the sample of planets with measured periods, radii and masses from the NASA Exoplanet Archive, and relative to the Neptune desert boundary of Mazeh et al. (2016). It can be seen that TOI-908 b lies just within the desert boundary.

4.3 Additional planets and TTVs

To evaluate the possible presence of additional planets in the system, both transiting and non-transiting, we implement additional searches of the *TESS* photometric data and the *HARPS* spectroscopic radial velocity data. We perform a BLS (Box Least Squares; Kovács, Zucker & Mazeh 2002) search on the *TESS* light-curve data with the transit model for TOI-908 b subtracted, and find no evidence of additional significant signals above a FAP of 0.1 besides the predicted rotation period of 20.53 d. We search the *HARPS* data using the DACE platform, which is capable of performing a periodogram
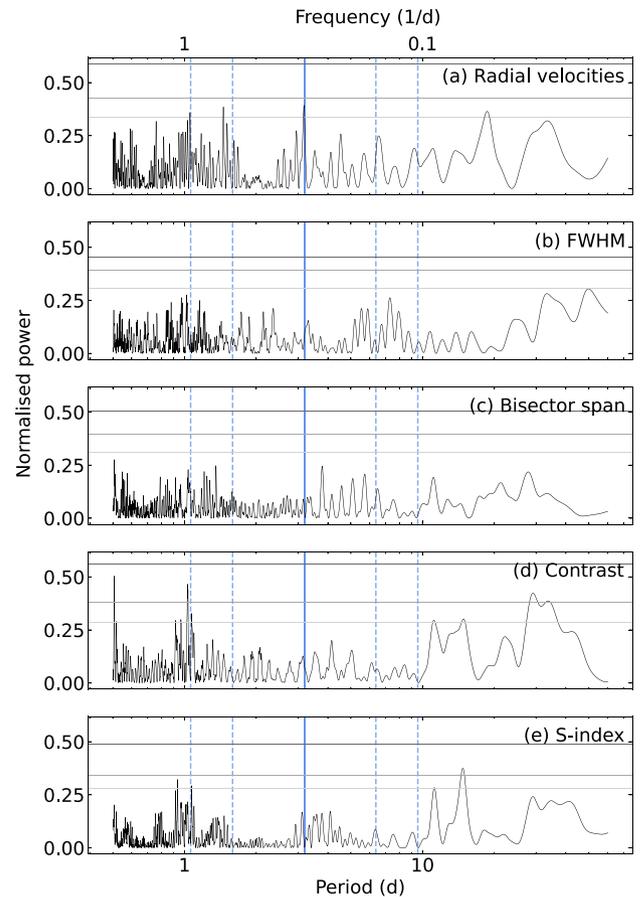
Figure 7. Periodograms for the *HARPS* radial velocity data of the values presented in Table 3. The orbital period of TOI-908 b is marked with a solid vertical blue line, alongside two period aliases either side of this value marked as dashed vertical blue lines. The FAPs are marked as the horizontal grey lines at 0.1, 1, and 10 per cent from top to bottom. *Panel 1*: Periodogram for the raw radial velocity data, with a peak at the orbital period value of TOI-908 b above the 0.1 per cent FAP line. *Panels 2–5*: Periodograms for the FWHM, bisector span, contrast, and S-index$_{MW}$.

search for additional periodic signals after the removal of the TOI-908 b radial velocity signal from the periodogram and the stellar rotation signal, and again we find no evidence for additional planets in the system. We also examine the individual transits from *TESS* and *LCOGT* with the EXOFAST[6] platform to model the measured central transit times T_{cm} and compare them with the calculated T_{cc}, and find that the measured transit times vary from the expected time by up to

---

[5] https://github.com/oscaribv/fancy-massradius-plot

[6] https://exoplanetarchive.ipac.caltech.edu/cgi-bin/ExoFAST/nph-exofast

Table 4. Stellar parameters of TOI-908.

Property (unit)	Value	Source
Mass ($M_\odot$)	0.950 ± 0.010	EXOPLANET
Radius ($R_\odot$)	1.028 ± 0.030	EXOPLANET
Density (g cm^{-3})	$1.235^{+0.091}_{-0.102}$	EXOPLANET
$P_{\rm rot}$ (d)	21.932 ± 6.167	EXOPLANET
LD coefficient u_1	0.296 ± 0.242	EXOPLANET
LD coefficient u_2	0.164 ± 0.291	EXOPLANET
$\log g$	4.45 ± 0.03	ARES + MOOG + *Gaia*
$T_{\rm eff}$ (K)	5626 ± 61	ARES + MOOG
$v\sin i_*$ (km s^{-1})	2.560 ± 0.636	ARES + MOOG
$v_{\rm turb}$ (km s^{-1})	0.913 ± 0.022	ARES + MOOG
Age (Gyr)	4.6 ± 1.5	Chemical clocks
Stellar abundances		
[Fe/H] (dex)	0.08 ± 0.04	ARES + MOOG
[C/H] (dex)	0.00 ± 0.03	ARES + MOOG
[O/H] (dex)	0.06 ± 0.13	ARES + MOOG
[Na/H] (dex)	0.10 ± 0.03	ARES + MOOG
[Mg/H] (dex)	0.10 ± 0.03	ARES + MOOG
[Al/H] (dex)	0.08 ± 0.04	ARES + MOOG
[Si/H] (dex)	0.07 ± 0.02	ARES + MOOG
[Ti/H] (dex)	0.09 ± 0.03	ARES + MOOG
[Ni/H] (dex)	0.07 ± 0.02	ARES + MOOG
[Cu/H] (dex)	0.08 ± 0.03	ARES + MOOG
[Zn/H] (dex)	0.05 ± 0.02	ARES + MOOG
[Sr/H] (dex)	0.16 ± 0.08	ARES + MOOG
[Y/H] (dex)	0.13 ± 0.07	ARES + MOOG
[Zr/H] (dex)	0.12 ± 0.03	ARES + MOOG
[Ba/H] (dex)	0.07 ± 0.04	ARES + MOOG
[Ce/H] (dex)	0.08 ± 0.02	ARES + MOOG
[Nd/H] (dex)	0.12 ± 0.03	ARES + MOOG

Sources. EXOPLANET (Foreman-Mackey et al. 2021a; Foreman-Mackey et al. 2021c), ARES (Sousa et al. 2015), MOOG (Sneden 1973b; Kurucz 1993b), *Gaia* (Brown et al. 2018).

29 min, consistent with our errors. We plot the TTVs for TOI-908 b in Fig. 11.

4.4 Internal structure modelling

We first estimate the internal structure of the planet assuming that it is comprised of a rocky core (Earth-like bulk density) surrounded by a H/He-rich envelope, following Rogers & Owen (2021). The internal structure can thus be described by four parameters: the core radius $R_{\rm core}$ and mass $M_{\rm core}$, the envelope radius $R_{\rm env}$, and the envelope mass fraction $f_{\rm env}$, which is defined in equation (4):

$$f_{\rm env} = \frac{M_{\rm env}}{M_{\rm p}} = \frac{M_{\rm p} - M_{\rm core}}{M_{\rm p}}, \qquad (4)$$

where $M_{\rm env}$ and $M_{\rm p}$ are the planet's envelope mass and total mass, respectively. We make use of the empirical mass–radius relations for rocky planets by Otegi, Bouchy & Helled (2020) to estimate the properties of the rocky core and relate core mass to core radius. For the H/He envelope, we adopt the envelope structure model by Chen & Rogers (2016), who provide a polynomial fit to their MESA simulations of the atmospheres of sub-Neptunes, in order to link envelope mass fraction and envelope radius. These formulations together reduce the number of unknowns to two: the envelope mass fraction and the core mass, which can be related to each other with the definition of envelope mass fraction above. The resulting internal structure, shown in Table 6, indicates an envelope mass fraction of
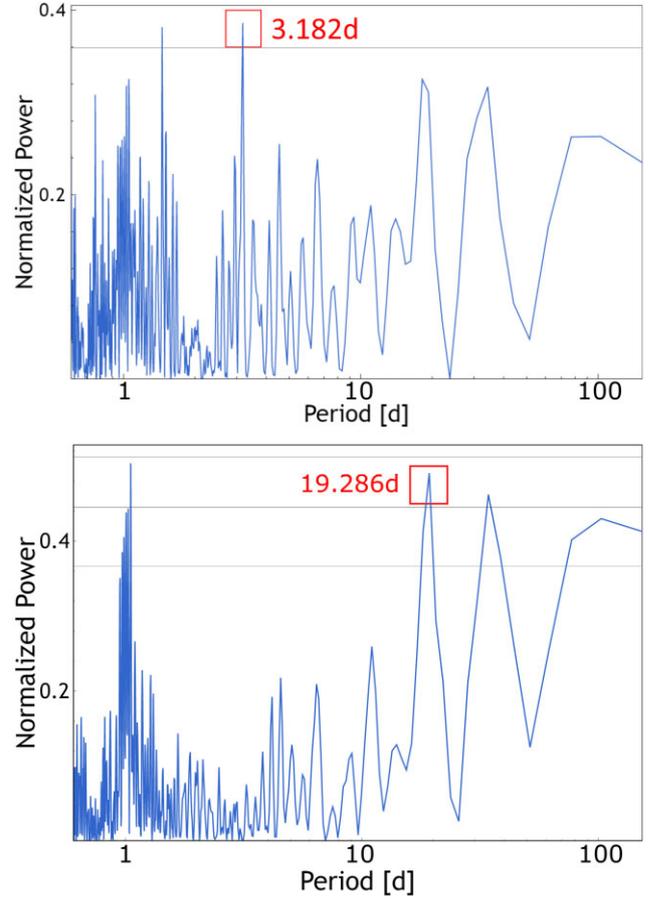
Figure 8. *Top panel:* Periodogram of the *HARPS* radial velocity data for TOI-908 showing the signal of TOI-908 b, marked with a red box. The horizontal line represents the 1 per cent FAP level. *Bottom panel:* Periodogram of the *HARPS* radial velocity data for TOI-908 with the signal of TOI-908 b removed, showing the remaining stellar rotational signal. The horizontal lines represent the 0.1 per cent, 1 per cent, and 10 per cent FAP levels.

Table 5. Parameters of TOI-908 b.

Property (unit)	Value
Catalog identifier	TOI-908.01
Period (d)	3.183792 ± 0.000007
Mass ($M_\oplus$)	$16.137^{+4.112}_{-4.039}$
Radius ($R_\oplus$)	3.186 ± 0.155
Density (g cm^{-3})	$2.742^{+0.241}_{-0.353}$
$R_{\rm p}/R_*$	0.028 ± 0.002
$T_{\rm c}$ (TBJD)	2384.292 ± 0.002
T1–T4 duration (h)	$2.457^{+0.120}_{-0.102}$
T2–T3 duration (h)	$2.268^{+2.225}_{-1.437}$
Impact parameter	0.536 ± 0.191
K (m s^{-1})	7.244 ± 1.768
Inclination ($^\circ$)	$86.475^{+1.258}_{-1.260}$
Semimajor axis (au)	0.041657 ± 0.000002
Temperature $T_{\rm eq}$ (K)[a]	1317 ± 38
Insolation flux ($S_\odot$)	80.884 ± 0.006
Eccentricity	0.132 ± 0.091
Argument of periastron ($^\circ$)	35.856 ± 94.972

[a] Assuming Albedo = 0 and uniform surface temperature.
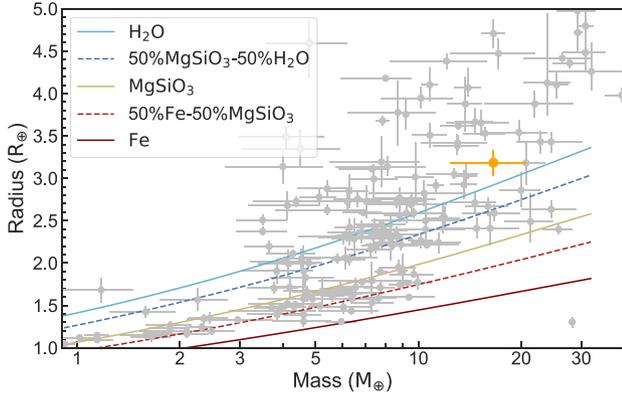
Figure 9. Mass–radius diagram showing the position of TOI-908 b (orange) among the population of exoplanets from the *TEPCAT* catalogue (Southworth 2011) (grey points), overplotted with composition models from Zeng, Sasselov & Jacobsen (2016).
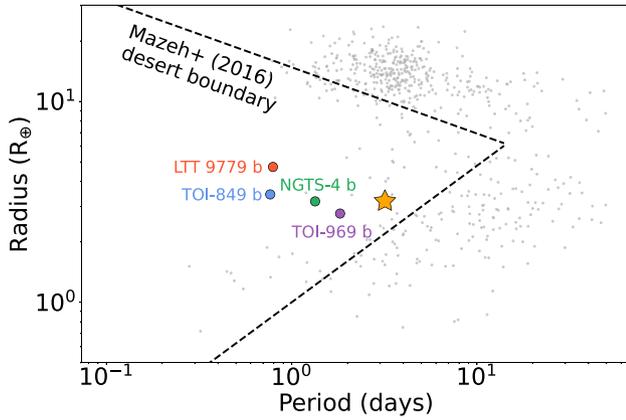
Figure 10. Plot showing the position of TOI-908 b (orange star) relative to the Neptune desert boundary of Mazeh et al. (2016), represented against the population of planets with measured periods and radii from the NASA Exoplanet Archive, and four confirmed planets in this parameter space: LTT 9779 b (Jenkins et al. 2020) (red circle), TOI-849 b (Armstrong et al. 2019) (blue circle), NGTS-4 b (West et al. 2019) (green circle), and TOI-969 b (Lillo-Box et al. 2022) (purple circle).
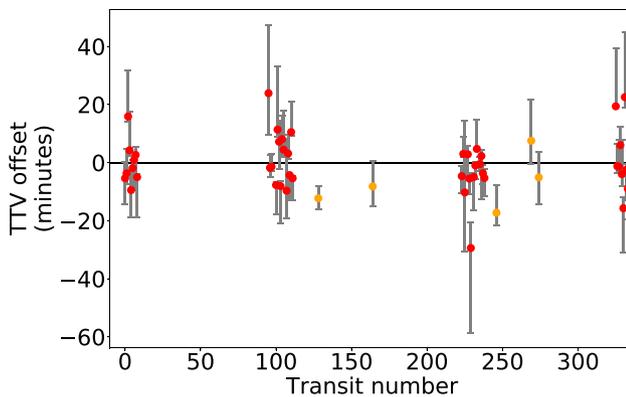
Figure 11. Transit timing varations (TTVs) for each transit of TOI-908 b from *LCOGT* (orange points), and each transit from *TESS* (red points), starting from transit number 0 taken as the first *TESS* transit in sector 1.

Table 6. Internal structure of TOI-908 b from Rogers & Owen (2021) models.

Property (unit)		Value
Core radius	R_{core} ($R_\oplus$)	2.31 ± 0.17
Core mass	M_{core} ($M_\oplus$)	16.0 ± 4.0
Envelope radius	R_{env} ($R_\oplus$)	0.87 ± 0.23
Envelope mass fraction	M_{env}/M_p	0.022 ± 0.010
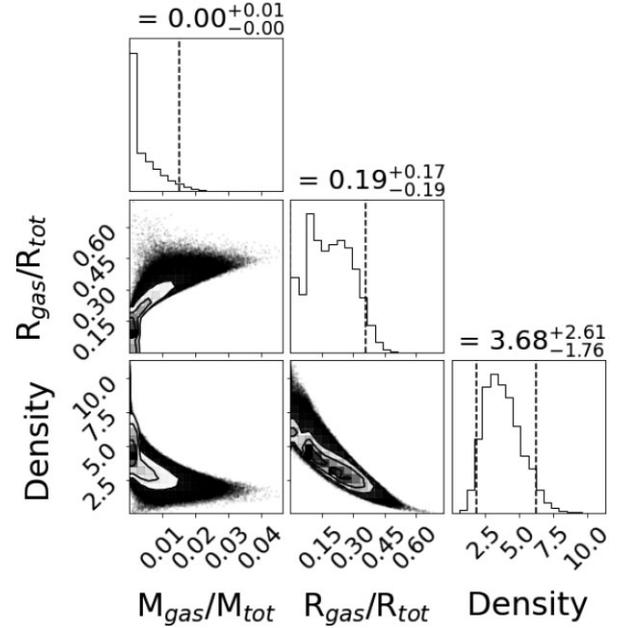
Figure 12. Corner plot of the derived internal structure parameters of TOI-908 b for the scenario with a water mass fraction of up to 0.5.

$f_{env} = 2.2 \pm 1.0$ per cent, typical of sub-Neptunes above the radius valley (Rogers & Owen 2021).

We perform an additional study of the internal structure of the planet with a Bayesian analysis, using the derived stellar and planetary properties. This method is described in details in Leleu et al. (2021a) and has been applied on several systems such as L98-59 (Demangeon et al. 2021), TOI-178 (Leleu et al. 2021a), or Nu2 Lupi (Delrez et al. 2021). In the model of planetary interior, four layers are assumed: a inner core made of iron and sulfur, a mantle of silicate (Si, Mg, and Fe), a water layer and a gaseous envelope of pure H–He. The core, mantle, and water layers form the 'solid' part of the planet and the thickness of the gaseous envelope depends on its mass and radius as well as the stellar age and irradiation (Lopez & Fortney 2014a). The resulting planetary parameters are the mass fraction of each layer, the iron molar fraction in the core, the silicon and magnesium molar fraction in the mantle, the equilibrium temperature, and the age of the planet (equal to the age of the star). Uniform priors are used for these parameters, except for the mass of the gas layer which is assumed to follow a uniform-in-log prior, with the water mass fraction having an upper boundary of 0.5 (Marboeuf et al. 2014; Thiabaud et al. 2014). For more details related to the connection between observed data and derived parameters, we refer to Leleu et al. (2021b). Two scenarios have been investigated for TOI-908 b: the case with water (water mass fraction up to 0.5) and the case without water. The Figs 12 and 13 refer to these two cases, respectively. Both cases give results consistent with the planetary observables. The case with water leads to an atmosphere representing 18 per cent of the total radius, whereas
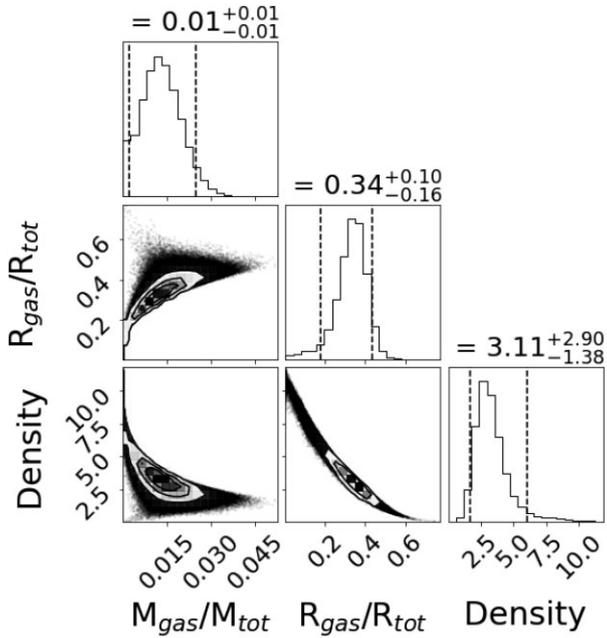
Figure 13. Corner plot of the derived internal structure parameters of TOI-908 b for the scenario with no water.

the case without water produces a thicker gaseous envelope of almost 35 per cent of the total radius.

4.5 Evaporation history of the planet

The Neptune desert and the radius valley are consistent with being the result of the evaporation of the atmospheres of sub-Neptunes (Lopez & Fortney 2013; Owen & Wu 2013; Jin et al. 2014; Lopez & Fortney 2014b). The underlying cause of evaporation is still under debate, though, and several mechanisms have been proposed. One such mechanism is photoevaporation, in which X-ray and extreme ultraviolet radiation (together, XUV), originating from the host star, provides the energy for evaporation (Watson, Donahue & Walker 1981; Erkaev et al. 2007). Photoevaporation

Table 7. Internal structure of TOI-908 b from Leleu et al. (2021b) models.

Property (unit)		Water	No water
Total radius	R_{tot} ($R_\oplus$)	2.9 ± 0.47	3.04 ± 0.46
Total mass	M_{tot} ($M_\oplus$)	16.5 ± 4.45	16.05 ± 4.79
Envelope radius	R_{env} ($R_\oplus$)	0.54 ± 0.6	1.02 ± 0.52
Envelope mass fraction	M_{env}/M_p	0.002 ± 0.010	0.010 ± 0.010

has been shown to reproduce both the radius valley (Rogers & Owen 2021) as well as the lower boundary of the Neptune desert (Owen & Lai 2018b). Ginzburg, Schlichting & Sari (2016) proposed an alternative mechanism for evaporation, core-powered mass loss, where the energy for atmospheric escape is provided by the internal thermal energy of the planet, and Gupta & Schlichting (2019) showed that it can also reproduce the radius-period valley. The existence of the radius valley has also been attributed to formation mechanisms (Zeng et al. 2019) and impacts by planetesimals (Wyatt, Kral & Sinclair 2020).

To study the evaporation history of the planet under this hypothesis, three ingredients are necessary: (1) a description of the XUV history of the star, (2) an envelope structure model (here we adopt Chen & Rogers 2016), and (3) a mass-loss model that relates the incident X-ray flux on the planet to the amount of mass lost.

The XUV history of a star can be estimated from its rotational history, as the two quantities are linked via the rotation–activity relation, where faster rotators produce higher X-ray fluxes (Wright et al. 2011, 2018). The X-ray luminosity of a star also declines with age, as stars spin down due to angular momentum loss through stellar winds (Jackson, Davis & Wheatley 2012; Tu et al. 2015; Johnstone et al. 2021). We adopt the rotational evolution models by Johnstone et al. (2021), who model the rotational spread and evolution of FGKM stars as a function of age and stellar mass. Fig. 14 shows the population mean and 2σ rotation tracks of a star of the mass of TOI-908, and their corresponding XUV tracks. Furthermore, we adopt the mass-loss formulation by Kubyshkina & Fossati (2021), based on hydrodynamic simulations of planetary atmospheres in the context of photoevaporation.

The model by Johnstone et al. (2021) predicts that a 0.95 $M_\odot$ star has an expected rotation period of 29 days, with a 2σ spread between
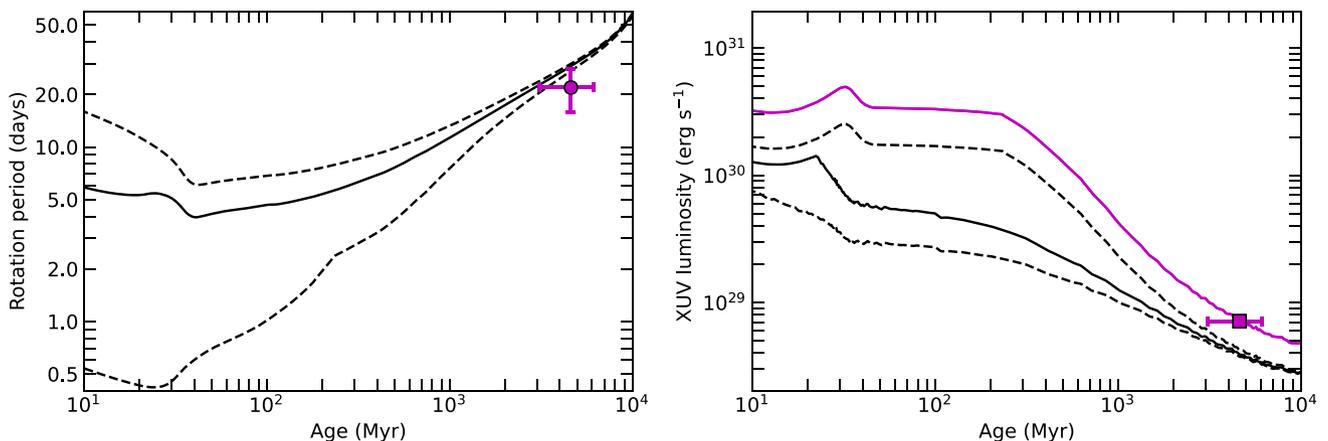
Figure 14. *Left-hand panel:* Plot showing the evolution of the rotation period of a 0.95 $M_\odot$ star using the initial rotation periods of the population mean (solid line) and the 2σ spread (dashed lines), following the model by Johnstone, Bartel & Güdel (2021). TOI-908, with a rotation period faster than expected for its age, is plotted as a purple circle. *Right-hand panel:* XUV evolution tracks of TOI-908 based on the rotational histories shown on the left-hand panel, together with the expected XUV luminosity of TOI-908, based on its rotation period (purple square), and the fitted XUV track to that value (purple line).
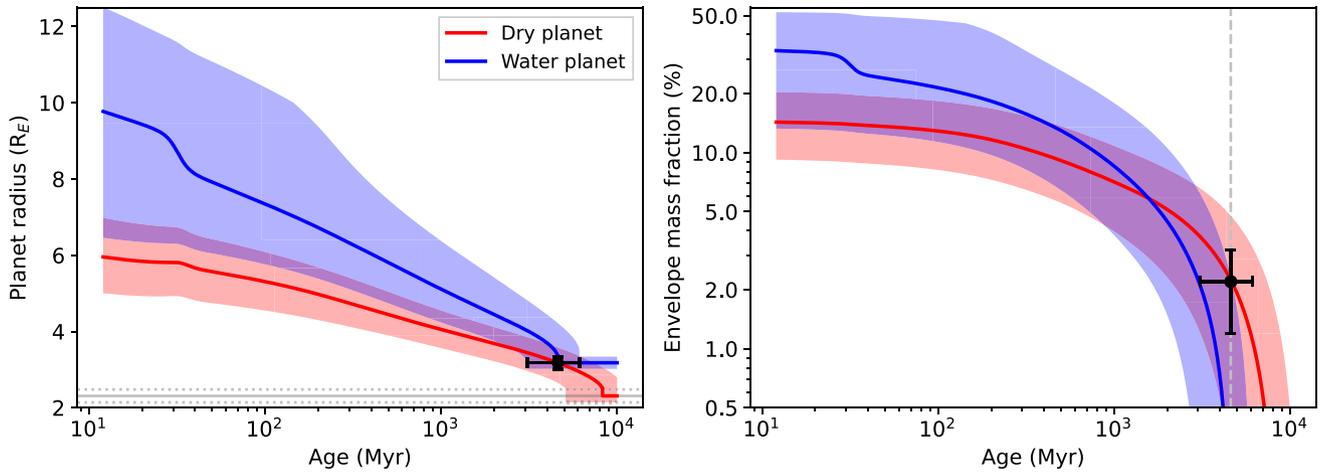
Figure 15. *Left-hand panel*: Plot showing the evolution of the radius of TOI-908 b using two models for the internal structure, one with a rocky core surrounded by gaseous atmosphere (red), and another with water instead of gas (blue). The shaded regions represent the spread in evaporation histories allowed by the 1σ uncertainties on the planet's mass, radius, and age. The present-day age and radius are shown with a black marker, and the rocky core radius (for the dry planet scenario) is shown as a horizontal grey line. *Right-hand panel*: Plot showing the evolution of the envelope mass fraction of TOI-908 b, akin to the left-hand panel. The present-day envelope mass fraction for the dry planet scenario is shown as a black circle, and the current age of the planet is plotted as a grey vertical line.

27 and 30 d, at an age of 4–5 Gyr. As shown in Fig. 14 (left-hand panel), TOI-908, with an age of 4.6 ± 1.5 Gyr, has a rotation period of 21.932 ± 6.167 d, which is a factor of ~ 1.5 times faster than predicted by the model, making the star an unusually fast rotator for its age. The 1σ uncertainties in the age and spin period, however, allow for younger and slower scenarios consistent with the spin evolution models. To model the XUV history of the star, we estimate the current X-ray luminosity using the rotation-activity relation, and use it to scale the model's 2σ upper limit X-ray track to fit our estimate, as shown in Fig. 14 (right-hand panel). Furthermore, we estimate the extreme ultraviolet (EUV) luminosity of the star using the empirical relations by King et al. (2018).

We simulate the evaporation history of TOI-908 b using the PHOTOEVOLVER code[7] (Fernández Fernández, Wheatley & King 2023), which evolves the planet's envelope by following these steps iteratively: first the current XUV flux on the planet is drawn from the stellar evolution tracks (see Fig. 14), then the mass-loss rate is obtained using the model by Kubyshkina & Fossati (2021), which is then subtracted from the envelope mass, and finally the envelope size is recalculated using the Chen & Rogers (2016) model and the simulation jumps to the next timestep. We run the simulation back to the age of 10 Myr and forward to 10 Gyr from the current age of 4.6 ± 1.5 Gyr under the XUV irradiation history motivated by the star's measured spin period. We simulated the evaporation past of the planet using the two internal structures we derived in Section 4.4: a rocky core surrounded by a gaseous envelope consisting of 2.2 ± 1.0 per cent of its mass, which we designated the *dry planet* scenario (shown in Table 6), and the Bayesian model by Leleu et al. (2021b) which accounts for the presence of water, and we designated the *water planet* scenario (shown in Table 7, left column). The results, shown in Fig. 15, indicate that in the dry planet scenario, TOI-908 b could have started out as a super-Neptune of radius 5–7 $R_\oplus$ and envelope mass fraction 10–20 per cent. On the other hand, we find that the evaporation past of the water scenario is fairly unconstrained, with initial states ranging from a 6.5 $R_\oplus$

planet akin to the initial state of the dry planet, to a puffy Jupiter-sized planet at 12 $R_\oplus$ with a significant envelope of mass fraction 50 per cent. Furthermore, we also find that the planet's envelope could be completely stripped by the age of 5–10 Gyr in the case of the dry planet, whereas the tenuous gas layer on the water planet is removed in tens to a hundred Myr.

5 CONCLUSION

We have presented the discovery of TOI-908 b, a hot sub-Neptune orbiting the G-type star TOI-908. We use a combination of transit photometry data from 6 sectors of *TESS* mission data at both 30 and 10 min cadence, further follow-up observations from the *LCOGT* telescope network, radial velocity data from *HARPS*, and *SOAR* speckle imaging to rule out the presence of blended companions. We jointly model our transit photometry and radial velocity data, and find that the planet orbits a G-type star with a radius of 0.95 ± 0.01 $M_\odot$ and a radius of 1.03 ± 0.03 $R_\odot$.

TOI-908 b has a radius of 3.18 ± 0.16 $R_\oplus$ and a mass of 16.1 ± 4.1 $M_\oplus$, with an orbital period of 3.18 d. It lies within the parameter space of the period-radius diagram known as the 'Neptune desert,' an area of parameter space where a dearth of planets is seen in current demographics. The mean density $2.7^{+0.2}_{-0.4}$ g cm^{-3} of TOI-908 b indicates an internal structure consisting of a core of radius ~ 2.3 $R_\oplus$ and mass of 16.0 $M_\oplus$, surrounded by an envelope of radius 0.87 $R_\oplus$ with a mass fraction of 2.2 per cent. Our analysis of the evaporation history of the planet indicates that its host star is rotating faster than expected, and predict that the planet was previously a super-Neptune of radius 5–7 $R_\oplus$ with an original envelope mass fraction of 10–20 per cent. Our models show the envelope will continue to evaporate in the future, and may be lost completely within the lifetime of the system. This planet is amenable to further follow-up with *JWST*, as despite its relatively low Transmission Spectroscopy Metric (TSM; Kempton et al. 2018) of 76 ± 6.7 it is a fairly bright ($T = 10.7$ mag) target undergoing atmospheric evaporation that lies close to the Continuous Viewing Zone of both *TESS* and *JWST* for ease of observation scheduling. This target should also be considered for further spectroscopic evaporation measurements via the metastable

[7]https://github.com/jorgefz/photoevolver

He-line (Oklopčić & Hirata 2018) with ground-based instruments, such as *CARMENES* or *NIRSPEC*.

DATA AVAILABILITY

The *TESS* data are accessible via the MAST (Mikulski Archive for Space Telescopes) portal at https://mast.stsci.edu/portal/Mashup/Clients/Mast/Portal.html. Photometry and imaging data from *LCOGT* and *SOAR* are accessible via the ExoFOP-*TESS* archive at https://exofop.ipac.caltech.edu/tess/target.php?id = 350153977. The EXOPLANET modelling code and associated PYTHON scripts for parameter analysis and plotting are available upon reasonable request to the author.

REFERENCES

Adibekyan V. Z., Sousa S. G., Santos N. C., Delgado Mena E., González Hernández J. I., Israelian G., Mayor M., Khachatryan G., 2012, A&A, 545, A32

Adibekyan V. et al., 2015, A&A, 583, A94

Agol E., Luger R., Foreman-Mackey D., 2020, AJ, 159, 123

Aller A., Lillo-Box J., Jones D., Miranda L. F., Barceló Forteza S., 2020, A&A, 635, A128

Armstrong D. J., Meru F., Bayliss D., Kennedy G. M., Veras D., 2019, ApJ, 880, L1

Armstrong D. J. et al., 2020, Nature, 583, 39

Astropy Collaboration, 2013, A&A, 558, A33

Astropy Collaboration, 2018, AJ, 156, 123

Bertran de Lis S., Delgado Mena E., Adibekyan V. Z., Santos N. C., Sousa S. G., 2015, A&A, 576, A89

Borucki W. J. et al., 2010, Science, 327, 977

Brown T. M. et al., 2013, PASP, 125, 1031

Brown A. et al., 2018, A&A, 616

Chen H., Rogers L. A., 2016, ApJ, 831, 180

Collins K. A., Kielkopf J. F., Stassun K. G., Hessman F. V., 2017, AJ, 153, 77

Delgado Mena E., Tsantaki M., Adibekyan V. Z., Sousa S. G., Santos N. C., González Hernández J. I., Israelian G., 2017, A&A, 606, A94

Delgado Mena E. et al., 2019, A&A, 624, A78

Delgado Mena E., Adibekyan V., Santos N. C., Tsantaki M., González Hernández J. I., Sousa S. G., Bertrán de Lis S., 2021, A&A, 655, A99

Delrez L. et al., 2021, Nat. Astron., 5, 775

Demangeon O. D. S. et al., 2021, A&A, 653, A41

Erkaev N. V., Kulikov Y. N., Lammer H., Selsis F., Langmayr D., Jaritz G. F., Biernat H. K., 2007, A&A, 472, 329

Fernández Fernández J., Wheatley P. J., King G. W., 2023, MNRAS, 522, 4251–4264

Foreman-Mackey D., Agol E., Ambikasaran S., Angus R., 2017, celerite: Scalable 1D Gaussian Processes in C++, Python, and Julia. preprint (ascl:1709.008)

Foreman-Mackey D. et al., 2021a, exoplanet-dev/exoplanet: exoplanet v0.4.5.

Foreman-Mackey D. et al., 2021b, exoplanet-dev/exoplanet: exoplanet v0.4.5.

Foreman-Mackey D. et al., 2021c, preprint (arXiv:2105.01994)

Gaia Collaboration, 2018, A&A, 616, A1

Ginzburg S., Schlichting H. E., Sari R., 2016, ApJ, 825, 29

Guerrero N. M. et al., 2021, ApJS, 254, 39

Gupta A., Schlichting H. E., 2019, MNRAS, 487, 24

Hawthorn F. et al., 2022, MNRAS, 520, 3649–3668

Henden A. A., Templeton M., Terrell D., Smith T. C., Levine S., Welch D., 2016, VizieR Online Data Catalog, II/336

Hoffman M. D., Gelman A., 2011, preprint (arXiv:1111.4246)

Jackson A. P., Davis T. A., Wheatley P. J., 2012, MNRAS, 422, 2024

Jenkins J. M., 2002, ApJ, 575, 493

Jenkins J. M. et al., 2010, in Radziwill N. M., Bridger A., eds, SPIE Conf. Ser. Vol. 7740, Software and Cyberinfrastructure for Astronomy. SPIE, Bellingham, 77400D

Jenkins J. M., Tenenbaum P., Seader S., Burke C. J., McCauliff S. D., Smith J. C., Twicken J. D., Chandrasekaran H., 2020, Kepler Data Processing Handbook: Transiting Planet Search, Kepler Science Document KSCI-19081-003.

Jensen E., 2013, Tapir: A Web Interface for Transit/Eclipse Observability. Astrophysics Source Code Library. preprint (ascl:1306.007)

Jin S., Mordasini C., Parmentier V., van Boekel R., Henning T., Ji J., 2014, ApJ, 795, 65

Johnstone C. P., Bartel M., Güdel M., 2021, A&A, 649, A96

Kempton E. M. R. et al., 2018, PASP, 130, 114401

King G. W. et al., 2018, MNRAS, 478, 1193

Kipping D. M., 2013a, MNRAS, 434, L51

Kipping D. M., 2013b, MNRAS, 435, 2152

Kovács G., Zucker S., Mazeh T., 2002, A&A, 391, 369

Kubyshkina D. I., Fossati L., 2021, Res Notes Am. Astron. Soc., 5, 74

Kumar R., Carroll C., Hartikainen A., Martin O. A., 2019, J. Open Source Softw

Kurucz R. L., 1993a, SYNTHE Spectrum Synthesis Programs and Line Data

Kurucz R. L., 1993b, Physica Scripta Volume T, 47, 110

Leleu A. et al., 2021a, A&A, 649, A26

Leleu A. et al., 2021b, A&A, 649, A26

Li J., Tenenbaum P., Twicken J. D., Burke C. J., Jenkins J. M., Quintana E. V., Rowe J. F., Seader S. E., 2019, PASP, 131, 024506

Lillo-Box J. et al., 2022, preprint (arXiv:2210.08996)

Lopez E. D., Fortney J. J., 2013, ApJ, 776, 2

Lopez E. D., Fortney J. J., 2014a, ApJ, 792, 1

Lopez E. D., Fortney J. J., 2014b, ApJ, 792, 1

Lovis C., Pepe F., 2007, A&A, 468, 1115

Luger R., Agol E., Foreman-Mackey D., Fleming D. P., Lustig-Yaeger J., Deitrick R., 2019a, aj, 157, 64

Luger R., Agol E., Foreman-Mackey D., Fleming D. P., Lustig-Yaeger J., Deitrick R., 2019b, AJ, 157, 64

Marboeuf U., Thiabaud A., Alibert Y., Cabral N., Benz W., 2014, A&A, 570, A36

Mayor M. et al., 2003, Messenger, 114, 20

Mazeh T., Holczer T., Faigler S., 2016, A&A, 589, A75

McCully C., Volgenau N. H., Harbeck D.-R., Lister T. A., Saunders E. S., Turner M. L., Siiverd R. J., Bowman M., 2018, Proc. SPIE, preprint (arXiv:1811.04163)

Oklopčić A., Hirata C. M., 2018, ApJ, 855, L11

Osborn A. et al., 2021, MNRAS, 507, 2782

Otegi J. F., Bouchy F., Helled R., 2020, A&A, 634, A43

Owen J. E., Lai D., 2018a, MNRAS, 479, 5012

Owen J. E., Lai D., 2018b, MNRAS, 479, 5012

Owen J. E., Wu Y., 2013, ApJ, 775, 105

Owen J. E., Wu Y., 2017, ApJ, 847, 29

Pepe F. et al., 2021, A&A, 645, A96

Ricker G. R. et al., 2015, J. Astron. Telesc. Instr. Syst., 1, 014003

Rogers J. G., Owen J. E., 2021, MNRAS, 503, 1526

Salvatier J., Wiecki T. V., Fonnesbeck C., 2016a, PeerJ Comput. Sci., 2, e55

Salvatier J., Wiecki T. V., Fonnesbeck C., 2016b, PeerJ Computer Science, 2, e55

Santos N. C. et al., 2013, A&A, 556, A150

Skrutskie M. F. et al., 2006, AJ, 131, 1163

Smith J. C. et al., 2012, PASP, 124, 1000

Sneden C. A., 1973a, PhD thesis, Univ. Texas at Austin

Sneden C. A., 1973b, PhD thesis, Univ. Texas at Austin

Sousa S. G., 2014, in Niemczura E., Smalley B., Pych W., eds, Determination of Atmospheric Parameters of B-, A-, F- and G-Type Stars. Springer International Publishing, Cham. p. 297

Sousa S. G., Santos N. C., Israelian G., Mayor M., Monteiro M. J. P. F. G., 2007, A&A, 469, 783

Sousa S. G., Santos N. C., Adibekyan V., Delgado-Mena E., Israelian G., 2015, A&A, 577, A67

Sousa S. G. et al., 2021, A&A, 656, A53

Southworth J., 2011, MNRAS, 417, 2166

Stassun K. G. et al., 2019, AJ, 158, 138

Stumpe M. C. et al., 2012, PASP, 124, 985

Stumpe M. C., Smith J. C., Catanzarite J. H., Van Cleve J. E., Jenkins J. M., Twicken J. D., Girouard F. R., 2014, PASP, 126, 100

Szabó G. M., Kiss L. L., 2011, ApJ, 727, L44

Theano Development Team, 2016, preprint (arXiv:1605.02688)

Thiabaud A., Marboeuf U., Alibert Y., Cabral N., Leya I., Mezger K., 2014, A&A, 562, A27

Tokovinin A., 2018, PASP, 130, 035002

Tu L., Johnstone C. P., Güdel M., Lammer H., 2015, A&A, 577, L3

Twicken J. D. et al., 2018, PASP, 130, 064502

Watson A. J., Donahue T. M., Walker J. C. G., 1981, Icarus, 48, 150

West R. G. et al., 2019, MNRAS, 486, 5094

Wright N. J., Drake J. J., Mamajek E. E., Henry G. W., 2011, ApJ, 743, 48

Wright N. J., Newton E. R., Williams P. K. G., Drake J. J., Yadav R. K., 2018, MNRAS, 479, 2351

Wyatt M. C., Kral Q., Sinclair C. A., 2020, MNRAS, 491, 782

Zeng L., Sasselov D. D., Jacobsen S. B., 2016, ApJ, 819, 127

Zeng L. et al., 2019, Proc. Natl. Acad. Sci., 116, 9723

Ziegler C., Tokovinin A., Briceño C., Mang J., Law N., Mann A. W., 2020, AJ, 159, 19

SUPPORTING INFORMATION

Supplementary data are available at *MNRAS* online.

Table 3. *HARPS* spectroscopic data for TOI-908.

Table A5. Additional *HARPS* activity indicator data for TOI-908.

Please note: Oxford University Press is not responsible for the content or functionality of any supporting materials supplied by the authors. Any queries (other than missing material) should be directed to the corresponding author for the article.

APPENDIX: PRIORS AND GP MODELS

Table A1. Global fit parameter prior function type and prior limits for TOI-908.

Parameter	Prior	Value
Baseline flux	$\mathcal{N}(0, 1)$	
M_* ($\mathrm{M}_\odot$)	$\mathcal{N}(0.95, 0.01, 0.95)$	Table 4
R_* ($\mathrm{R}_\odot$)	$\mathcal{N}(1.03, 0.03, 1.03)$	Table 4
P_{rot} (d)	$\mathcal{N}(20.53, 7.00)$	Table 4
LD coefficient u_1	Kipping (2013b)	Table 4
LD coefficient u_2	Kipping (2013b)	Table 4

Notes. Numbers in brackets represent:
(mean μ, standard deviation σ, test value α) for normal distribution $\mathcal{N}(\mu, \sigma, \alpha)$.
Distributions for limb darkening coefficients u_1 and u_2 are built into the EXOPLANET package and based on Kipping (2013b).

Table A2. Global fit parameter prior function type and prior limits for TOI-908 b.

Parameter	Prior	Value
TOI-908b		
Period (d)	$\mathcal{N}(3.1837961, 0.0000112)$	Table 5
Transit ephemeris (TBJD)	$\mathcal{U}(2384.25, 2384.33)$	Table 5
$\log(R_{\mathrm{p}})$	$\mathcal{N}(-3.549^a, 1)$	Table 5 (R_{p})
Impact parameter	$\mathcal{U}(0, 1)$	Table 5
Eccentricity	Kipping (2013a), $\mathcal{B}(e, 0.867, 3.03)$	Table 5
Argument of periastron (rad)	$\mathcal{U}(-\pi, \pi)$	Table 5 ($°$)

Notes. Numbers in brackets represent:
(mean μ, standard deviation σ) for normal distribution $\mathcal{N}(\mu, \sigma)$.
(lower limit x, upper limit y) for uniform distribution $\mathcal{U}(x,y)$.
^{a}Equivalent to $0.5\times\log(\delta) + \log(R_*)$, δ represents transit depth (based on ExoFOP catalogue values).
Distributions for eccentricity e are built into the EXOPLANET package and based on Kipping (2013a) which includes the Beta distribution $\mathcal{B}(e, a, b)$ (exponential e, shape parameter a, shape parameter b).

Table A3. Global fit parameter prior function type and prior limits for *TESS* photometric data.

Parameter	Prior	Value
Sector 1		
Mean	$\mathcal{N}(0, 1)$	-0.00001 ± 0.00009
$\log(s2)$	$\mathcal{N}(-15.536^a, 0)$	-15.781 ± 0.039
$\log(w0)$	$\mathcal{N}(0, 0.1)$	0.104 ± 0.095
$\log(Sw4)$	$\mathcal{N}(-15.536^a, 0)$	-15.574 ± 0.096
Sector 12		
Mean	$\mathcal{N}(0, 1)$	-0.00001 ± 0.00008
$\log(s2)$	$\mathcal{N}(-15.702^a, 0.1)$	-15.822 ± 0.043

Table A3 *– continued*

Parameter	Prior	Value
$\log(w0)$	$\mathcal{N}(0, 0.1)$	0.132 ± 0.100
$\log(Sw4)$	$\mathcal{N}(-15.702^a, 0.1)$	-15.757 ± 0.100
Sector 13		
Mean	$\mathcal{N}(0, 1)$	0.00004 ± 0.00014
$\log(s2)$	$\mathcal{N}(-15.183^a, 0.1)$	-15.609 ± 0.040
$\log(w0)$	$\mathcal{N}(0, 0.1)$	0.019 ± 0.088
$\log(Sw4)$	$\mathcal{N}(15.183^*, 0.1)$	-15.162 ± 0.095
Sector 27		
Mean	$\mathcal{N}(0, 1)$	0.00007 ± 0.00033
$\log(s2)$	$\mathcal{N}(-13.932^a, 0.1)$	-14.357 ± 0.027
$\log(w0)$	$\mathcal{N}(0, 0.1)$	0.056 ± 0.094
$\log(Sw4)$	$\mathcal{N}(-13.932^a, 0.1)$	-13.411 ± 0.109
Sector 28		
Mean	$\mathcal{N}(0, 1)$	0.00007 ± 0.00015
$\log(s2)$	$\mathcal{N}(-14.578^a, 0.1)$	-14.646 ± 0.025
$\log(w0)$	$\mathcal{N}(0, 0.1)$	0.139 ± 0.103
$\log(Sw4)$	$\mathcal{N}(-14.578^a, 0.1)$	-14.646 ± 0.098
Sector 39		
Mean	$\mathcal{N}(0, 1)$	0.00002 ± 0.00012
$\log(s2)$	$\mathcal{N}(-14.656^a, 0.1)$	-14.743 ± 0.022
$\log(w0)$	$\mathcal{N}(0, 0.1)$	0.185 ± 0.104
$\log(Sw4)$	$\mathcal{N}(-14.656^a, 0.1)$	-14.761 ± 0.099

Notes. Numbers in brackets represent:
(mean μ, standard deviation σ) for normal distribution $\mathcal{N}(\mu, \sigma)$.
Prior values:
^{a}Equivalent to the log of the variance of the *TESS* flux from the corresponding sector.

Table A4. Global fit parameter prior function type and prior limits for *HARPS* radial velocity data.

Parameter	Prior	Value
K (m s^{-1})	$\mathcal{U}(0, 10)$	Table 5
Amplitude	$\mathcal{C}(5)$	6.321 ± 2.657
l_E	$\mathcal{T}(20.53, 20, 20)$	34.982 ± 11.285
l_P	$\mathcal{T}(0.1, 10, 0, 1)$	0.640 ± 0.209
HARPS offset	$\mathcal{N}(9102.921^a, 10)$	9103.035 ± 3.808
$\log(\mathrm{Jitter}_{HARPS})$	$\mathcal{N}(1.293^b), 5)$	-4.528 ± 2.708

Notes. Numbers in brackets represent:
(lower limit x, upper limit y) for uniform distribution $\mathcal{U}(x,y)$.
(scale parameter β) for half-Cauchy distribution $\mathcal{C}(\beta)$.
(mean μ, standard deviation σ, lower limit x, upper limit y) for truncated normal distribution $\mathcal{T}(\mu, \sigma, x, y)$.
(mean μ, standard deviation σ) for normal distribution $\mathcal{N}(\mu, \sigma)$.
Prior values:
^{a}Equivalent to the mean of the *HARPS* radial velocity.
^{b}Equivalent to 2 times the log of the minimum *HARPS* radial velocity error

Table A5. Additional *HARPS* activity indicator data for TOI-908. This table is available in its entirety online.

Hα-index	H α index error	Na index	Na index error	Ca index	Ca index error
0.003024	0.000001	0.264718	0.001861	0.121843	0.004656
0.002718	0.000001	0.260553	0.001679	0.132003	0.004192
0.002366	0.000001	0.263481	0.001440	0.132657	0.003269
0.002739	0.000001	0.260150	0.001688	0.121485	0.004012
0.002411	0.000001	0.261340	0.001464	0.139120	0.003539
...	...	...	...	...	...

Table A6. All TTVs from *TESS*.

Transit no.	TTV (mins)	Transit no.	TTV (mins)
0	$-5.4^{+8.9}_{-5.6}$	223	$-4.7^{+5.7}_{-3.6}$
1	$-3.7^{+3.5}_{-8.4}$	224	$3.0^{+1.0}_{-5.7}$
2	$15.9^{+1.8}_{-15.9}$	225	$-10.3^{+20.3}_{-24.7}$
3	$4.2^{+1.8}_{-13.2}$	227	$2.9^{+6.6}_{-3.0}$
4	$-9.5^{+9.4}_{6.86.8}$	228	$-5.5^{+5.5}_{-1.3}$
5	$-1.9^{+7.6}_{-3.0}$	229	$-29.4^{+29.2}_{-8.8}$
6	$0.9^{+10.2}_{-1.5}$	231	$-5.0^{+11.3}_{-1.2}$
7	$2.6^{+8.1}_{-2.8}$	232	$-1.0^{+4.7}_{-1.2}$
8	$-5.0^{+13.9}_{-1.1}$	233	$4.7^{+0.3}_{-10.1}$
95	$23.9^{+14.3}_{-23.6}$	235	$-0.5^{+2.5}_{-2.5}$
96	$-1.8^{+3.0}_{-4.4}$	236	$2.3^{+14.9}_{-2.3}$
97	$-1.4^{+1.6}_{-4.6}$	237	$-3.7^{+3.6}_{-2.8}$
100	$-7.7^{+10.2}_{-1.1}$	238	$-5.3^{+6.4}_{-6.4}$
101	$11.4^{+2.5}_{-21.9}$	325	$19.4^{+0.1}_{-20.1}$
102	$7.2^{+9.6}_{-7.1}$	326	$-1.2^{+2.2}_{-7.6}$
103	$-8.1^{+12.7}_{-1.6}$	327	$-1.4^{+1.4}_{-9.2}$
104	$8.1^{+6.1}_{-7.9}$	328	$6.0^{+3.6}_{-6.2}$
105	$4.5^{+2.4}_{-13.5}$	329	$-4.0^{+4.0}_{-11.9}$
107	$-9.7^{+9.6}_{-17.7}$	330	$-15.7^{+15.4}_{-3.8}$
108	$3.1^{+1.8}_{-6.6}$	331	$22.5^{+3.7}_{-22.3}$
109	$-4.3^{+8.7}_{-0.2}$	332	$-2.5^{+10.4}_{-1.8}$
110	$10.5^{+1.3}_{-10.5}$	333	$-9.0^{+10.4}_{-0.4}$
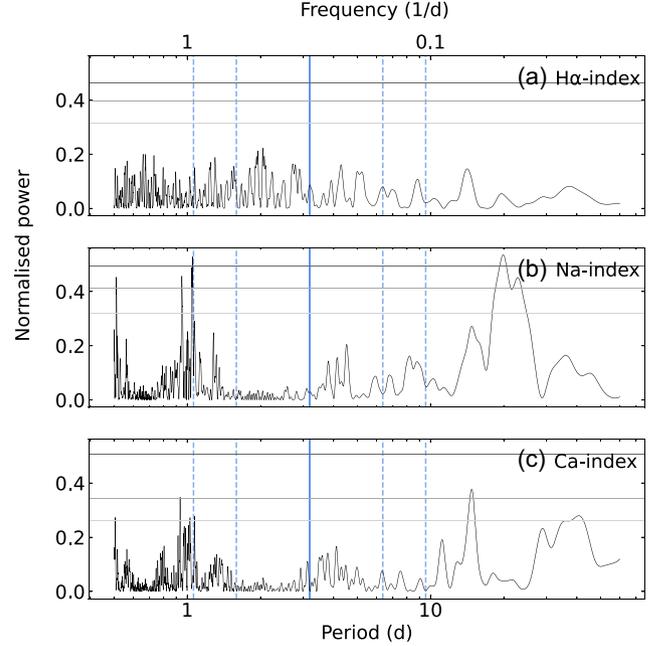
Figure A1. Periodograms for the *HARPS* radial velocity data of the values presented in Table A5. The orbital period of TOI-908 b is marked with a solid vertical blue line, alongside two period aliases either side of this value marked as dashed vertical blue lines. The FAPs are marked as the horizontal grey lines at 0.1, 1, and 10 per cent from top to bottom. *Panels 1-3*: Periodograms for the H α index, Na index, and Ca index.
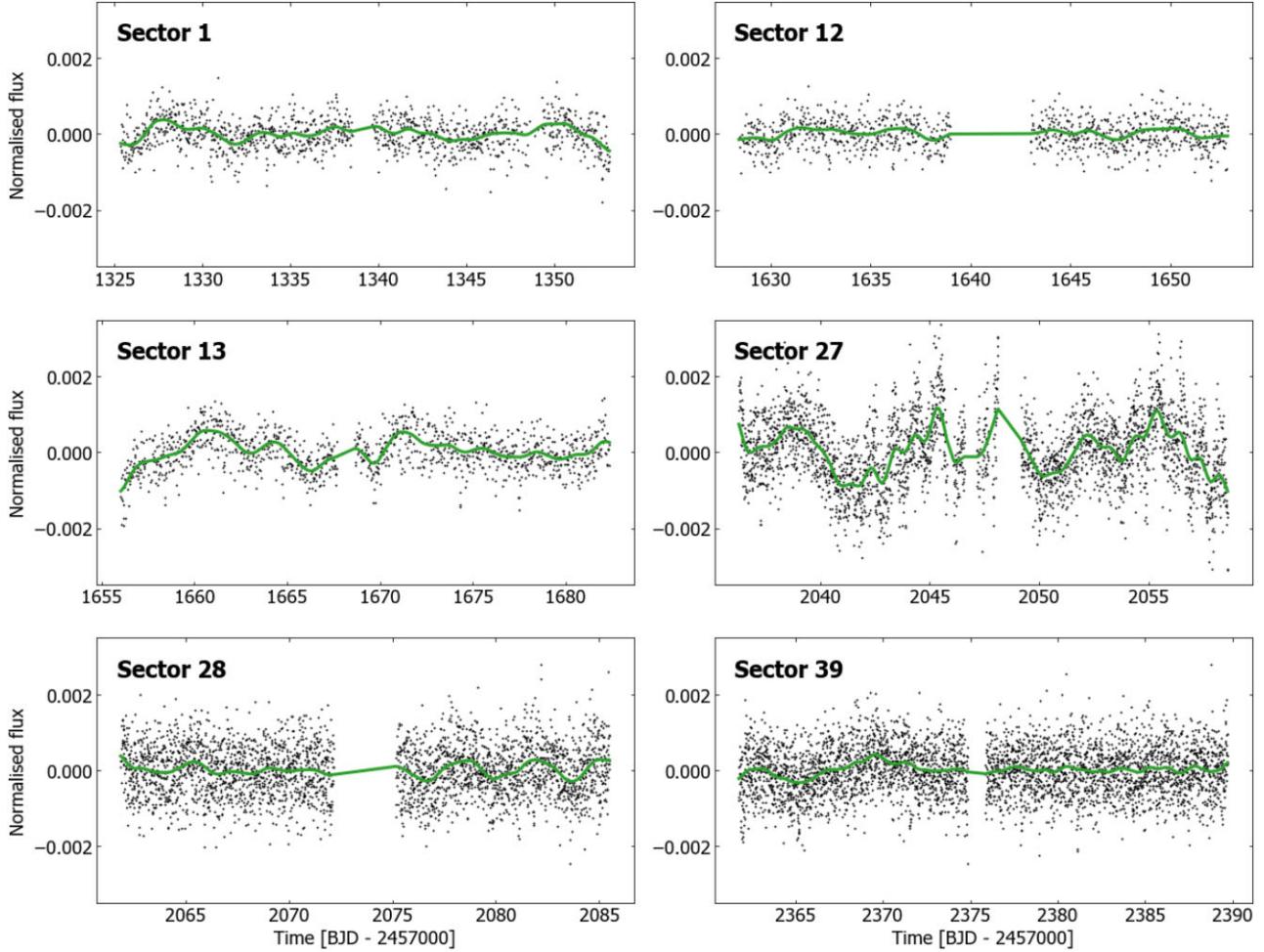
Figure A2. *TESS* PDCSAP light curves from labelled sectors, overplotted with the GP models in green.

[1]*Department of Physics, University of Warwick, Gibbet Hill Road, Coventry CV4 7AL, UK*

[2]*Centre for Exoplanets and Habitability, University of Warwick, Gibbet Hill Road, Coventry CV4 7AL, UK*

[3]*Instituto de Astrofísica e Ciências do Espaço, Universidade do Porto, CAUP, Rua das Estrelas, PL-4150-762 Porto, Portugal*

[4]*Departamento de Física e Astronomia, Faculdade de Ciências, Universidade do Porto, Rua do Campo Alegre, PL-4169-007 Porto, Portugal*

[5]*Physikalisches Institut, University of Bern, NCCR PlanetS, CSH, Gesellschaftsstrasse 6, CH-3012 Bern, Switzerland*

[6]*Center for Astrophysics | Harvard & Smithsonian, 60 Garden Street, Cambridge, MA 02138, USA*

[7]*Observatoire de l'Université de Genève, Chemin Pegasi 51, 1290 Versoix, Switzerland*

[8]*INAF-Osservatorio Astrofisico di Torino, Via Osservatorio 20, I-10025 Pino Torinese, Italy*

[9]*IPAC-NASA Exoplanet Science Institute, 770 S. Wilson Avenue, Pasadena, CA 91106, USA*

[10]*Department of Astrophysical Sciences, Princeton University, Princeton, NJ 08544, USA*

[11]*International Center for Advanced Studies (ICAS) and ICIFI (CONICET), ECyT-UNSAM, Campus Miguelete, 25 de Mayo y Francia, 1650 Buenos Aires, Argentina*

[12]*Department of Astronomy and Tsinghua Centre for Astrophysics, Tsinghua University, Beijing 100084, China*

[13]*SUPA Physics and Astronomy, University of St Andrews, Fife, KY16 9SS Scotland, UK*

[14]*Aix Marseille Univ, CNRS, CNES, LAM, 13388 Cedex 13 Marseille, France*

[15]*NASA Ames Research Center, Moffett Field, CA 94035, USA*

[16]*Department of Physics & Astronomy, Swarthmore College, Swarthmore PA 19081, USA*

[17]*Department of Physics and Astronomy, University of Louisville, Louisville, KY 40292, USA*

[18]*NASA Goddard Space Flight Center, 8800 Greenbelt Rd, Greenbelt, MD 20771, USA*

[19]*Department of Physics and Kavli Institute for Astrophysics and Space Research, Massachusetts Institute of Technology, Cambridge, MA 02139, USA*

[20]*Centro de Astrobiología (CAB, CSIC-INTA), Depto. de Astrofísica, ESAC campus, E-28692, Villanueva de la Cañada (Madrid), Spain*

[21]*European Southern Observatory, Karl-Schwarzschild-Straße 2, D-85748 Garching bei München, Germany*

[22]*Department of Earth, Atmospheric, and Planetary Sciences, Massachusetts Institute of Technology, Cambridge, MA 02139, USA*

[23]*Department of Aeronautics and Astronautics, Massachusetts Institute of Technology, Cambridge, MA 02139, USA*

[24]*Facultad de Ciencias Astronómicas y Geofísicas, Universidad Nacional de La Plata, Paseo del Bosque s/n, B1900 Buenos Aires, Argentina*

[25]*Hazelwood Observatory, Churchill, Victoria, Australia*

[26]*SETI Institute, Mountain View, CA 94043, USA*

[27]*Department of Physics, Engineering and Astronomy, Stephen F. Austin State University, 1936 North Street, Nacogdoches, TX 75962, USA*

This paper has been typeset from a TEX/LATEX file prepared by the author.